CHALMERS
UNIVERSITY OF TECHNOLOGY

Environment-Aware Channel Measurement and Modeling for Terahertz Monostatic Sensing

Citation for the original published paper (version of record):
Lyu, Y., Yuan, Z., Wymeersch, H. et al (2026). Environment-Aware Channel Measurement and Modeling for Terahertz Monostatic Sensing. IEEE Transactions on Wireless Communications, 25: 13369-13383. http://dx.doi.org/10.1109/TWC.2026.3671384

Environment-Aware Channel Measurement and Modeling for Terahertz Monostatic Sensing

Yejian Lyu, Zhiqiang Yuan, Henk Wymeersch, *Fellow, IEEE*, and Chong Han, *Senior Member, IEEE*

***Abstract*—Integrated sensing and communication (ISAC) at terahertz (THz) frequencies holds significant promise for unifying ultra-high-speed wireless connectivity with fine-grained environmental awareness. Realistic and interpretable channel modeling is essential to fully realize the potential of such systems. This work presents a comprehensive investigation of monostatic sensing channels at 300 GHz, based on an extensive measurement campaign conducted at 57 co-located transceiver (TRx) positions across three representative indoor scenarios. Multipath component (MPC) parameters, including amplitude, delay, and angle, are extracted using a high-resolution space-alternating generalized expectation-maximization (SAGE) algorithm. To cluster the extracted MPCs, an image-processing-based clustering method, i.e., connected component labeling (CCL), is applied to group MPCs based on delay-angle consistency. Based on the measurement data, an environment-aware channel modeling framework is proposed to establish mappings between physical scenario attributes (e.g., reflector geometry, surface materials, and roughness) and their corresponding channel-domain manifestations. The framework incorporates both specular and diffuse reflections and leverages several channel parameters, e.g., reflection loss, Lambertian scattering, and intra-cluster dispersion models, to characterize reflection behavior. Experimental results demonstrate that the proposed approach can reliably extract physical characteristics, e.g., structural and material information, from the observed channel characteristics, offering a promising foundation for advanced THz ISAC channel modeling.**

***Index Terms*—Terahertz, monostatic sensing, environment-aware channel modeling.**

I. Introduction

INTEGRATED sensing and communication (ISAC) is a key enabler for sixth-generation (6G) and beyond wireless systems, allowing networks to sense and interpret their physical environment [1]–[4]. The advancement of terahertz (THz) technology has further extended ISAC capabilities to high-resolution tasks such as human activity recognition, automotive radar, and indoor mapping [5]–[7]. The THz band, spanning 100 GHz to 10 THz, offers ultra-wide bandwidth and sub-millimeter wavelengths that, together with large antenna arrays or highly directional antennas, enable fine delay and angular resolution [8], [9]. These frequencies have also attracted growing interest from international standardization bodies. IEEE Std. 802.15.3d specifies the first low-THz communication physical layer in the 252–325 GHz band, while the Federal Communication Commission (FCC) expanded spectrum licenses for the spectrum above 95 GHz in 2019 [10]. European Telecommunications Standards Institute Industry Specification Group-THz (ETSI-ISG-THz) and International Telecommunication Union (ITU)-R have initiated studies on THz use cases, spectrum ranges, and regulatory considerations [11], [12]. These efforts also underscore several propagation challenges unique to the THz band, including severe free-space path loss, strong molecular absorption, pronounced blockage sensitivity, and a distinct balance between specular and diffuse scattering. Such characteristics make the THz channel highly dependent on local geometry and material properties, thereby reinforcing the need for precise, measurement-based modeling to fully capture its behavior. Despite these challenges, THz signals provide a favorable trade-off between spatial resolution and propagation robustness when compared with microwave and free-space optical systems. Their sub-millimeter wavelengths enable fine-grained delay and angular discrimination beyond what microwave systems can offer, while avoiding the strong weather susceptibility and line-of-sight dependence characteristic of optical links. This combination makes the THz band particularly well-suited for radio-based environmental sensing in complex indoor scenarios.

Accurate and reliable channel modeling serves as a critical foundation for designing and evaluating emerging wireless communication systems, especially those integrating sensing functionalities [19]. Wireless sensing scenarios are generally classified based on transmitter (Tx) and receiver (Rx) placement into two main configurations: monostatic, where Tx and Rx share the same location, and bistatic, where they occupy distinct spatial positions [20]. Compared to conventional bistatic communication channels, which exhibit complex multipath propagation due to separated Tx-Rx links, monostatic sensing channels primarily involve direct reflections, both specular and diffuse, from environmental objects [21]. These structural differences lead to fundamentally distinct delay–angle behaviors and scattering characteristics. In a monostatic configuration, the Tx and Rx share the same phase center, resulting in identical angles of departure and arrival for each MPC. This symmetry simplifies geometric interpretation and enables direct observation of material-dependent backscattering properties, including the angular decay of reflection strength and the balance between specular and diffuse components—features that are much more difficult to isolate in bistatic setups. Moreover, monostatic sensing is also the widely adopted architecture in ISAC systems at sub-6 GHz and millimeter-wave frequencies [22]–[25], and this device-centric sensing paradigm naturally extends to THz deployments [16], [17], [26]. In practical ISAC scenarios, such as indoor access

Y. Lyu and C. Han are with the Terahertz Wireless Communications Laboratory at Shanghai Jiao Tong University, Shanghai 200240, China (e-mail: {yejian.lyu; chong.han}@sjtu.edu.cn);

Z. Yuan and H. Wymeersch are with the Communication Systems Group at Chalmers University of Technology, Gothenburg, Sweden.

TABLE I
SUMMARY OF STATE-OF-THE-ART THZ SENSING CHANNEL MEASUREMENTS AND MODELING

Ref.	Frequency	Sensing Mode	Scenario	Analysis
[13]	130-143 GHz	Monostatic & bistatic	Indoor & outdoor	Scatterer-based hybrid ISAC model
[14]	190 GHz	Bistatic	Factory	Scatterer detection based on power-angle spectrum
[15]	306-321 GHz	Monostatic	Empty room & corridors	Ranging accuracy and back-scattering coefficient
[16]	235-320 GHz	Monostatic	Laboratory	SLAM-based mapping and tracking
[17]	290-310 GHz	Monostatic	Laboratory	THz hybrid sensing channel model
[18]	290-310 GHz	Monostatic	Laboratory	Centimeter-level Environment reconstruction
This work	290-310 GHz	Monostatic	Three distinct indoor scenarios	Cluster-based environment-aware channel models for THz sensing

points, XR wearables, and autonomous robotic platforms, a single device is often required to perform high-precision environment awareness without relying on external synchronization. As a result, accurate characterization of monostatic THz sensing channels is essential for understanding the sensing-oriented propagation behaviors that uniquely arise at THz frequencies.

Current research on monostatic and bistatic ISAC channel modeling remains limited. Early studies investigated combined bistatic and monostatic links at 140 GHz, proposing hybrid deterministic-stochastic models to characterize ISAC propagation in indoor and outdoor environments [13]. Bistatic sensing measurements in industrial scenarios have demonstrated the feasibility of high-resolution detection of environmental scatterers [14]. Indoor monostatic channel measurements between 306 and 321 GHz evaluated ranging accuracy and backscattering behavior in empty rooms and corridors [15]. Recent work employing radio simultaneous localization and mapping at 235-320 GHz further showcased the potential of monostatic transceiver position tracking and environment mapping [16]. A geometry-based stochastic channel model has been proposed in [27], providing a practical support for ISAC system design by accurately characterizing complex propagation environments and preserving essential geometric relationships. In our prior work [17], indoor monostatic sensing channel measurements were carried out at 290-310 GHz, where a hybrid modeling approach was proposed: diffuse components were exploited for environmental reconstruction, while specular reflections enabled preliminary material identification. Building on this foundation, environment reconstruction using the same dataset was further implemented and evaluated in [18]. The summary of the current state of the art in THz ISAC channel measurement and modeling is provided in Table I.

Despite considerable progress in the above literature, several key aspects remain insufficiently addressed. First, although THz bistatic channel studies have advanced rapidly, measurements and modeling of THz monostatic sensing channels remain relatively limited. Second, the detailed identification and analysis of cluster-level channel characteristics—including intra-cluster delay and angular spreads, power distributions, and reflection-loss statistics—are still underexplored in the context of THz sensing, constraining the fidelity of existing models. Third, while prior studies have examined material properties at THz frequencies [18], [28]–[31], they seldom establish explicit links between physical environmental attributes (e.g., geometry, surface roughness, and material composition) and their corresponding delay–angle–power signatures in the THz band.

To address these gaps, this work conducts extensive monostatic sensing measurements at 300 GHz across three representative indoor scenarios and develops a novel environment-aware modeling framework that directly connects physical material characteristics with their channel-domain manifestations. Notably, compared with our earlier works [17], [18], which were confined to a single measurement environment and limited material identification (cement versus metal only), this work significantly expands both the data and analytical scope. It incorporates new datasets collected across diverse indoor scenarios and examines a broad set of common materials, including metal, glass, polymer, cement, and tile. Moreover, it introduces a generalized framework that jointly captures geometric, material, and angular–power behaviors of both specular and diffuse components, enabling a more comprehensive interpretation of THz monostatic sensing channels. These extensions substantially deepen the analysis beyond our prior work and provide a more complete foundation for material-aware THz channel modeling. The key contributions of this paper are summarized as follows:

- A comprehensive THz monostatic sensing measurement dataset is presented at the 300 GHz band, collected across three structurally and materially diverse indoor scenarios with 57 co-located TRx positions. Unlike prior datasets that are limited to simplified or homogeneous scenarios, the proposed dataset captures a rich variety of spatial, geometric, and material characteristics, including metallic, dielectric, and composite surfaces. The dataset provides a valuable foundation for advancing research in channel modeling, material-aware sensing, localization, and ISAC.
- This work advances THz monostatic sensing analysis by characterizing multipath component (MPC) clusters rather than only TRx-specific metrics as in [17]. Using space-alternating generalized expectation-maximization (SAGE)-extracted MPCs, we analyze cluster-wise delay and angular characteristics and develop a statistical channel model that incorporates both global and intra-cluster properties. This model enables more realistic evaluations of ISAC sensing performance.
- Building on the statistical cluster-based channel characterization, we develop an environment-aware channel modeling framework for monostatic sensing, which explicitly links physical characteristics of the environment, such as material type, surface roughness, object geome-

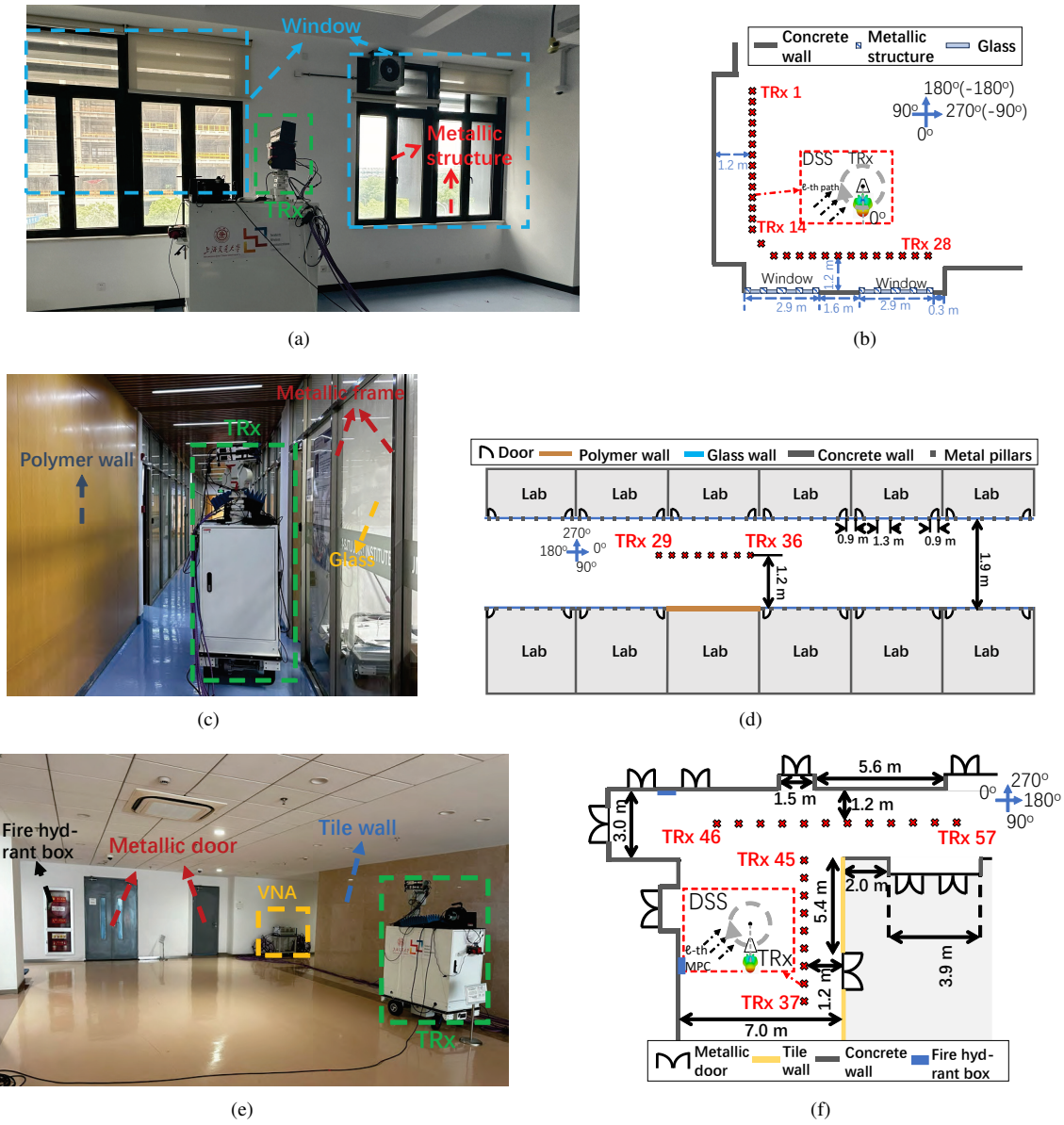

Fig. 1. Diagrams and photos of the measurement scenario for THz monostatic sensing. (a) Real photo in Scenario 1. (b) Diagram of Scenario 1. (c) Real photo in Scenario 2. (d) Diagram of Scenario 2. (e) Real photo in Scenario 3. (f) Diagram of Scenario 3.

try, and scene complexity, to corresponding propagation features.

The remainder of this paper is structured as follows. Section II outlines the monostatic-sensing-based measurement setup and scenario. The data processing and image-processing-assisted cluster identification method are described in Section III. The indoor channel characterization for THz monostatic sensing is presented in Section IV. Besides, a material-related modeling framework is proposed in in Section V. Finally, concluding remarks are presented in Section VI.

II. Measurement Campaign

In this section, we present the details of the THz monostatic channel measurement campaign. We begin by describing the measurement system setup, including the system configuration, antenna specifications, and calibration procedures. Subsequently, we introduce the three representative indoor scenarios used in the campaign, highlighting their spatial dimensions, layout structures, and dominant material compositions.

A. Sounder and Measurement Setup

In this work, a vector network analyzer (VNA)-based channel sounder [32], [33] operating from 290 to 310 GHz is employed for monostatic sensing channel measurements. The system provides an ultra-wide bandwidth of 20 GHz, corresponding to a fine delay resolution of approximately 1.5 cm in the delay domain. A total of 2001 frequency points are sampled, supporting a maximum detectable range of 30 m. To ensure a high dynamic range and measurement accuracy, the intermediate frequency (IF) bandwidth is configured at 1 kHz.

TABLE II
THE MONOSTATIC SENSING CHANNEL MEASUREMENT CONFIGURATION FOR THE THREE SCENARIOS.

Parameter	Value
Frequency range	290-310 GHz
Frequency bandwidth	20 GHz
Frequency point	2001
Transmission power	10 dBm
Noise floor	-170 dB
Maximum detectable distance	30 m
IF bandwidth	1 kHz
Tx & Rx antenna type	Horn
Antenna gain	25.5 dBi
Azimuthal HPBW	8°
Rotation step	1°
Azimuthal rotation range	$[0^\circ : 359^\circ]$
Tx Antenna height	2.0 m
Rx Antenna height	2.1 m

As illustrated in Fig. 1, the co-located Tx and Rx are mounted on a precision-controlled turntable to mimic monostatic sensing conditions. Identical high-gain horn antennas are used at both ends, featuring 25.5 dBi gain and a narrow half-power beamwidth (HPBW) of 8°, enabling high angular resolution. The directional scanning sounding (DSS) scheme is applied to capture rich azimuthal characteristics, with antenna rotation covering $[0^\circ, 359^\circ]$ in fine 1° increments, offering dense angular sampling. The antenna phase center is positioned 0.2 m from the rotation axis to avoid mechanical shadowing and maintain spatial consistency. The Tx and Rx are set at heights of 2.0 m and 2.1 m, respectively. This slight vertical offset results from the mechanical design of the Tx/Rx extenders and does not affect the measurements, as the platform performs azimuth-only rotation with a fixed elevation angle. Furthermore, the small LoS coupling component between the co-located Tx and Rx is removed through a time-gating procedure, ensuring that all extracted MPCs originate solely from environmental scattering. Prior to measurements, full system calibration is performed using a back-to-back setup to remove system response and ensure accurate channel estimation. A summary of key measurement parameters is provided in Table II.

B. Measurement Scenario

In this work, comprehensive monostatic channel measurements are conducted across three representative indoor scenarios to characterize diverse propagation conditions relevant to THz ISAC systems. Scenario 1 represents an indoor laboratory environment with an L-shaped measurement trajectory, as illustrated in Fig. 1 (a) and (b). Along this route, a total of 28 TRx positions are uniformly spaced at intervals of 0.5 m. As highlighted in Fig. 1 (b), the primary reflective objects in Scenario 1 include a flat cement wall and two metal-framed windows. The readers can refer to our previous work [17] for a detailed description of this scenario.

Scenario 2 captures a narrow corridor scenario with a width of 1.9 m. One side of the corridor is constructed with large glass panels supported by multiple small metal pillars, while the opposite side is a polymer wall. As depicted in Fig. 1 (c) and (d), eight TRx locations are placed along the corridor at 1 m intervals and a fixed distance of 1.2 m to the polymer wall, capturing the wave interactions with the polymer, transparent, and metallic materials under quasi-parallel wall alignment.

Scenario 3 represents an L-shaped hallway with a more complex architectural layout. The scenario features a mix of surface types, including concrete walls, ceramic tile finishes, fire hydrant boxes, and metallic doors, offering diverse reflection characteristics, as shown in Fig. 1 (e) and (f). In this scenario, 21 TRx locations are positioned along a 'T'-shaped measurement route with a uniform spacing of 1 m between adjacent points, enabling high spatial resolution for geometry-aware analysis. To ensure a fair comparison of material-related channel parameters under consistent geometric conditions, the distance between the TRx and the flat wall is deliberately fixed at 1.2 m across all three scenarios. Note that this controlled setup isolates the impact of wall material by eliminating distance- and geometry-induced variability, and it does not imply a limitation of the proposed model to fixed-distance configurations.

These scenarios encompass a wide range of material types, including metal, polymer, cement, tile, and glass, along with representative indoor reflector geometries such as flat walls, concave corners, and convex corners. In total, channel measurements are performed at 57 co-located TRx positions. At each position, 360 angular measurements are taken, resulting in a total of $57 \times 360 = 20520$ channel frequency responses (CFRs) across the three indoor environments. These environments exhibit diverse surface materials, structural geometries, and spatial layouts, providing a dataset for THz monostatic channel analysis.

III. Data Processing and Analysis

This section outlines the signal processing approach for the measured data. It starts with the introduction of the signal model for the monostatic sensing case. Using this model, key MPC parameters are extracted through a SAGE-based parameter estimation algorithm. Subsequently, an image-based method is applied to detect and group the MPC clusters.

A. Signal Model

The directional CFR in the rotation angle of θ in the m^{th} location can be expressed as

$$H_m(f,\theta) = \sum_{\ell=1}^{L_m} \alpha_\ell \exp(-j2\pi f \tau_\ell) \cdot a_{\text{TRx},\phi_\ell}(f,\theta), \quad (1)$$

where α_ℓ, τ_ℓ, ϕ_ℓ, and f denote the complex amplitude (capturing both power attenuation and initial propagation phase), the delay, the azimuth angle of the ℓ^{th} path, and the carrier frequency, respectively. Note that in this work, we assume that the departure azimuth angle and impinge azimuth angle are the same as ϕ_ℓ for the ℓ^{th} path. L_m represents the total number of MPCs. $a_{\text{TRx},\phi_\ell}(f,\theta)$ is the rotation manifold coefficient, which contains the phase difference caused by DSS and the antenna pattern for ℓ^{th} path, and can be written as

$$a_{\text{TRx},\phi_\ell}(f,\theta) = \left[\exp(j2\pi f r \cos(\theta)/\text{c})\right]^2 \cdot G_{\text{TRx}}(f, \phi_\ell - \theta), \quad (2)$$

where r and c represent the azimuthal distance from the antenna phase center to the rotation center and the speed of light, respectively. $G_{\mathrm{TRx}}(f, \phi_\ell - \theta)$ is the complex radiation pattern of the mimic monostatic sensor. In this paper, a trajectory-tracking-assisted SAGE algorithm in [17] is employed to de-embed the antenna patterns and extract the MPC parameters, i.e., amplitude, delay, and angle, from the measurement data. The extracted parameter set $\hat{\Theta}^{(m)}$ in the m^{th} location can be expressed as

$$\hat{\Theta}^{(m)} = \begin{bmatrix} \hat{\alpha}_1^{(m)} & \cdots & \hat{\alpha}_\ell^{(m)} & \cdots & \hat{\alpha}_{Lm}^{(m)} \\ \hat{\tau}_1^{(m)} & \cdots & \hat{\tau}_\ell^{(m)} & \cdots & \hat{\tau}_{Lm}^{(m)} \\ \hat{\phi}_1^{(m)} & \cdots & \hat{\phi}_\ell^{(m)} & \cdots & \hat{\phi}_{Lm}^{(m)} \end{bmatrix}, \tag{3}$$

where $\hat{\alpha}_\ell^{(m)}$, $\hat{\tau}_\ell^{(m)}$, and $\hat{\phi}_\ell^{(m)}$ denote the extracted amplitude, delay, and azimuth angle of ℓ^{th} MPC, respectively.

B. Image-processing-based Cluster Identification

After extracting the MPC parameters from the measurement data using SAGE algorithm, an image-processing-based method is used to identify the MPC clusters in the measured power-angle-delay profiles (PADPs) of each TRx location. The measured CFR $H_m(f, \theta)$ in the m^{th} location is first transformed to channel impulse response (CIR) $h_m(\tau, \theta)$ through the inverse discrete Fourier transform (IDFT). Then, the PADP $\mathrm{PADP}(\tau, \theta)$ can be obtained as

$$\mathrm{PADP}(\tau, \theta) = 20 \cdot \log_{10}\left(|\mathrm{h}(\tau, \theta)|\right). \tag{4}$$

The signal region $S(\tau, \theta)$ is first constructed based on the PADP as

$$S(\tau, \theta) = \begin{cases} 1, & \text{if } \mathrm{PADP}(\tau, \theta) > T \\ 0, & \text{otherwise} \end{cases}, \tag{5}$$

where T denotes the signal threshold. In this work, T is set to be 10 dB above the noise floor [17]. Here, the $\mathrm{PADP}(\tau, \theta)$ represents the power distribution in the delay–angle domain, and $S(\tau, \theta)$ is obtained by applying a threshold to $\mathrm{PADP}(\tau, \theta)$, effectively serving as its binary segmentation mask that isolates significant signal regions from background noise.

To enhance the connectivity of detected signal regions and suppress small-scale noise, a morphological closing operation is applied to the binary signal map, which is widely used in the image processing domain [34], [35]. This yields a refined region $S_{\mathrm{closed}}(\tau, \theta)$ defined as:

$$S_{\mathrm{closed}}(\tau, \theta) = (S(\tau, \theta) \oplus \mathcal{K}) \ominus \mathcal{K}, \tag{6}$$

where $\oplus$ and $\ominus$ denote the dilation and erosion operations, respectively, and $\mathcal{K} \subseteq \mathbb{Z}^2$ is a predefined structuring element. Here, $\mathbb{Z}^2$ refers to all 2D grid points with integer coordinates.

Let $A \subseteq \mathbb{Z}^2$ denote a detected signal region on the delay-angle domain. The dilation operation $\oplus$ expands the boundaries of A, which can be expressed as

$$A \oplus \mathcal{K} = \{z \in \mathbb{Z}^2 \mid (\mathcal{K}^* + z) \cap A \neq \emptyset\}, \tag{7}$$

where z is a candidate grid position, and $\mathcal{K}^* = \{-k \mid k \in \mathcal{K}\}$ denotes the the symmetric of $\mathcal{K}$. The notation $\mathcal{K}^* + z$ represents a spatial shift of $\mathcal{K}^*$ by vector z.

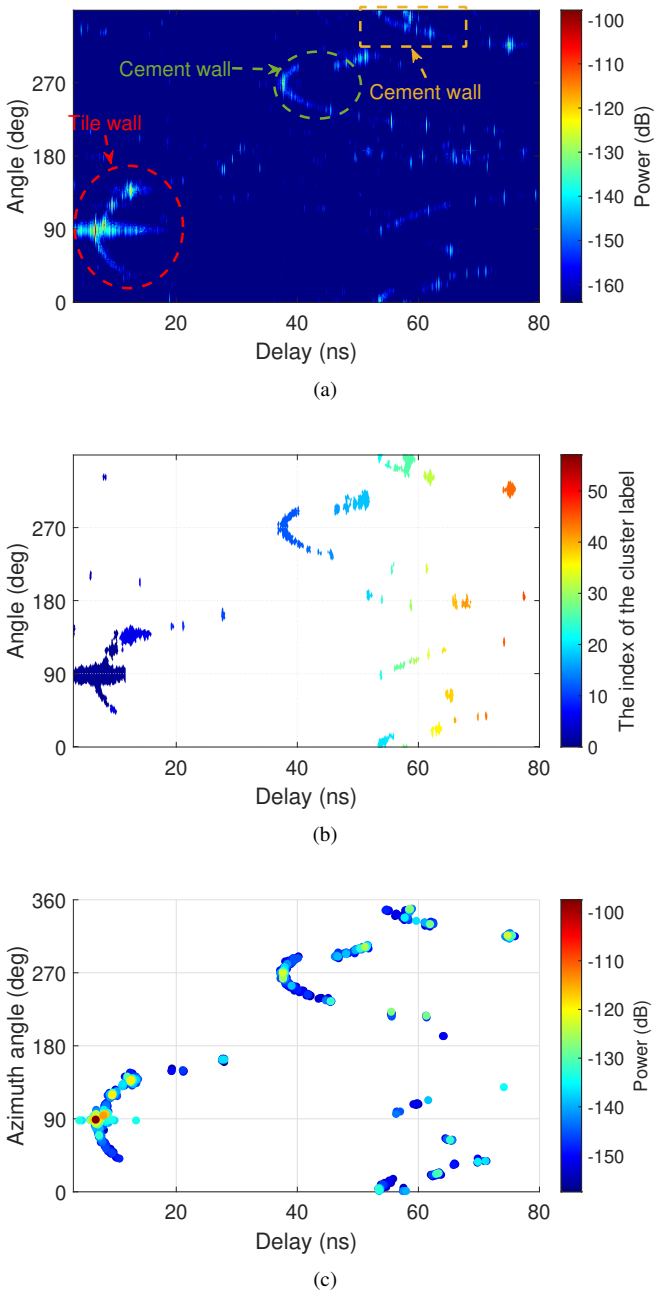

Fig. 2. Results of PADP, identified MPC clusters, and the estimated MPCs. (a) Exemplary PADP in TRx 40. (b) Identified MPC clusters after CCL in TRx 41. (c) Estimated MPCs by SAGE algorithms.

In contrast, the erosion operation $\ominus$ shrinks the boundaries of A, removing small, isolated components and smoothing edges, which can be defined as

$$A \ominus \mathcal{K} = \{z \in \mathbb{Z}^2 \mid (\mathcal{K} + z) \subseteq A\}. \tag{8}$$

Subsequently, a connected component labeling (CCL) algorithm is applied to segment contiguous signal regions, where each region is defined as a group of adjacent foreground pixels that share the same label [36]. To eliminate spurious noise, regions with fewer than $N_{\min}$ pixels are discarded. The i^{th} delay-angle cluster region $\mathcal{C}_i$ is defined as:

$$\mathcal{C}_i = \{(\tau,\theta) \mid I(\tau,\theta) = i,\ S(\tau,\theta) = 1\}, \tag{9}$$

where $I(\tau,\theta)$ denotes the labeled image, which assigns label i to the point (τ,θ).

Finally, the union of all valid cluster regions can be expressed as

$$\mathcal{C} = \bigcup_{i}^{I} \mathcal{C}_i. \tag{10}$$

Fig. 2 presents an example of the PADP and the corresponding MPC clusters identified using the CCL algorithm and the estimated MPC after using the SAGE algorithm in [17]. As shown in Fig. 2 (a), the primary structural features of the scenario, such as the tile and cement walls, are clearly visible. The application of CCL enables effective segmentation of the MPC clusters, as illustrated in Fig. 2 (b). Besides, the MPCs are accurately estimated from the measured CFR data, as depicted in Fig. 2 (c).

To justify the number of extracted MPCs and the resulting cluster formations, we cross-checked our observations with representative THz measurement studies. Across the THz literature, it is well established that each physical scatterer generates multiple resolvable MPCs due to the millimeter-scale wavelength and strong diffuse-scattering behavior. Vegetation produces abundant diffuse components [37], indoor 300 GHz measurements reveal dense diffuse-scattering clouds around dominant reflections [38], [39], and data-center measurements report several to dozens of MPCs per reflector [40]. Even outdoor THz campaigns [41] observe distinct diffuse clusters around walls and corners. These findings confirm that the MPC counts in our measurements fall within the expected ranges.

A key distinction from prior works lies in the cluster structure. Most existing THz studies employ bistatic or communication-oriented geometries [42]–[44], where Tx and Rx are separated, causing clusters to mix contributions from multiple surfaces due to differing angle-of-departure and angle-of-arrival viewpoints. In contrast, our monostatic configuration ensures that each physical reflector produces a compact and geometrically coherent cluster that aligns directly with its spatial footprint. This compactness and structural consistency motivate the use of an image-processing-based connected-component labeling (CCL) method rather than conventional distance-based clustering approaches such as K-means, which assume centroid-shaped clusters. The CCL method identifies spatially connected reflection regions in the delay–angle domain, allowing elongated or curved MPC distributions arising from physical reflector geometries to be preserved. This yields more structure-aware and physically interpretable cluster representations.

IV. Cluster-Based Channel Characterization

This section analyzes the channel characteristics of monostatic sensing at the 300 GHz band across the three indoor scenarios. In this context, a cluster denotes a group of MPCs exhibiting relative proximity in delay and angular domains, generally resulting from specular and diffuse reflections off one or more closely spaced reflectors [45], [46]. These MPCs are perceived as a coherent group in the delay-angle domain and collectively characterize the channel response associated with a local scattering region in the environment.

A. Identification of the Specular and Diffuse Components

In monostatic sensing channels, specular and diffuse reflections constitute the primary propagation mechanisms. Reflection loss serves as a distinguishing parameter between specular and diffuse components within MPC clusters, which are predominantly composed of specular reflections. In our analysis, specular components are identified by their relatively lower reflection losses and alignment with strong, geometrically consistent propagation paths, whereas diffuse components exhibit higher losses and broader angular spreads. A threshold is selected based on the statistical distribution of reflection losses observed across the dataset. The reflection loss $Loss_\ell$ for ℓ^{th} de-embedded MPC can be expressed as

$$Loss_\ell[\text{dB}] = \text{FSPL}_\ell[\text{dB}] - 20 \cdot \log_{10} |\hat{\alpha}_\ell|, \tag{11}$$

where FSPL_ℓ (in decibels) is the free space path loss through the propagation channel. The free space path loss FSPL_ℓ can be calculated as

$$\text{FSPL}_\ell = 20 \cdot \log_{10} \left(\frac{4\pi f_c d_\ell}{\text{c}} \right), \tag{12}$$

with f_c denoting the centering frequency, and $d_\ell = \hat{\tau}_\ell^{(m)} \cdot c$ representing the round trip propagation distance of ℓ^{th} path.

The exemplary reflection loss results are shown in Fig. 3. As illustrated in Fig. 3 (a), each identified cluster typically contains a dominant specular MPC characterized by low reflection loss, along with multiple diffuse MPCs exhibiting higher reflection losses. The probability density functions (PDFs) of reflection loss for Clusters 1 and 2 are shown in Fig.3(b). In Cluster 1, the specular MPC exhibits the lowest reflection loss of 2.5 dB, while the reflection losses of diffuse MPCs span a wide range from 27 to 69 dB. In Cluster 2, the reflection loss of the specular MPC is 10.49 dB, and that of the diffuse MPCs ranges from 20 to 45 dB. These results provide physical insight into the underlying propagation mechanisms, i.e., specular MPCs arise from strong, geometrically aligned reflections with minimal scattering loss, while diffuse MPCs are caused by interactions with rough or irregular surfaces that scatter energy over wider angular ranges, resulting in higher reflection losses. The clear separation in reflection loss between specular and diffuse components indicates that reflection loss is a reliable and interpretable metric for classifying multipath components in THz monostatic sensing channels.

B. Number of MPC Clusters

The number of MPC clusters serves as an important metric for analyzing the complexity of a propagation environment. In this work, the number of MPC clusters is examined across three indoor scenarios. Specifically, in Scenario 3, TRxs 37-45 and TRxs 46-57 are treated as two distinct cases. The cumulative distribution functions (CDFs) of the number of MPC clusters are presented in Fig. 4. It can be observed that Scenario 1 and TRxs 37-45 exhibit a similar number

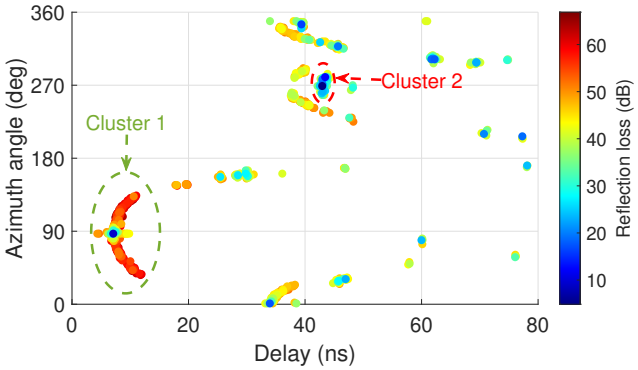

(a)

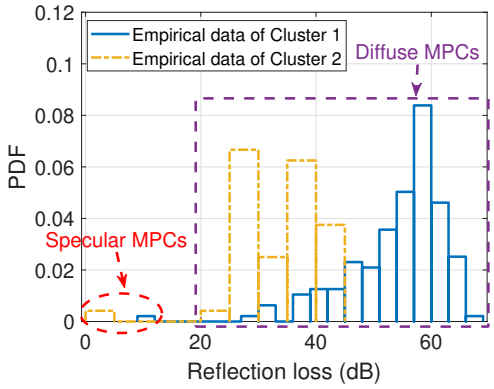

(b)

Fig. 3. Exemplary results of reflection loss analysis. (a) The comparison of the reflection loss and MPC distribution at TRx 41. (b) PDF of the reflection loss for MPC clusters at TRx 41.

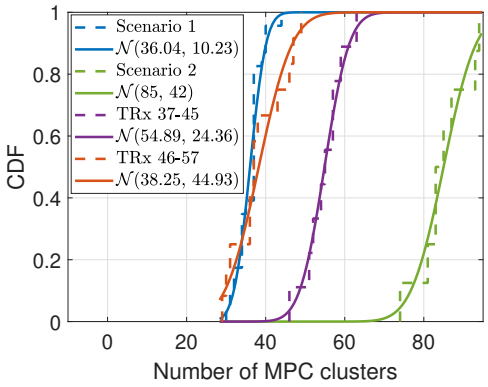

Fig. 4. The CDF of the number of MPC clusters and the fitted models.

of MPC clusters. TRxs 37-45 is shown to have a higher number of clusters compared to those in Scenario 1 and TRxs 37-45. In contrast, Scenario 2 has the highest number of MPC clusters among all cases, which can be attributed to the presence of more metallic structures that act as strong reflectors. The CDFs of the number of clusters in the four cases align well with normal distributions, characterized by the parameters $\mathcal{N}(36.01, 10.23)$, $\mathcal{N}(85, 42)$, $\mathcal{N}(54.89, 24.36)$, and $\mathcal{N}(38.25, 44.93)$, respectively, as illustrated in Fig. 4.

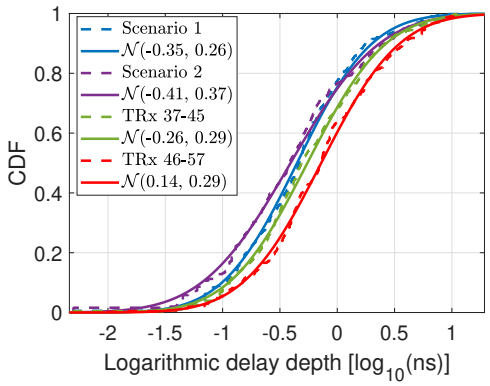

(a)

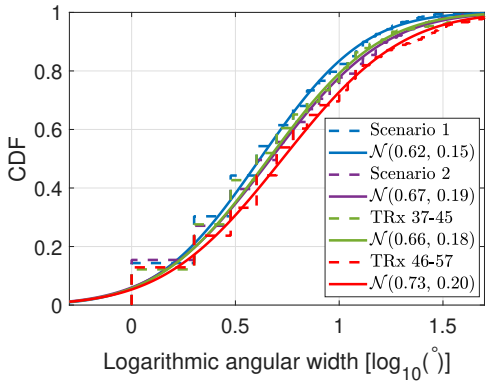

(b)

Fig. 5. The CDF of the logarithmic intra-cluster delay depth, logarithmic angular width, and the fitted models. (a) Delay depth. (b) Angular width.

C. Intra-Cluster Delay and Angular Characteristics

The channel characteristics in the delay and angle domains are essential for characterizing the shape of MPC clusters, which in turn reflect the size and geometry of reflectors present in the environment. In this work, we characterize cluster parameters using four key intra-cluster metrics: delay depth, angular width, delay spread, and angular spread. In this work, delay depth is defined as the total delay range between the earliest and latest arrived MPCs within a cluster, describing the full temporal extent of the cluster. Angular width refers to the difference between the minimum and maximum angles of arrival of the MPCs in the cluster, representing its overall angular coverage. For clarity, delay depth and delay spread describe different delay-domain properties: the former measures the full delay extent, whereas the latter quantifies the statistical dispersion of delays around the mean. Similarly, angular width describes the geometric angular extent, while angular spread characterizes the dispersion of arrival angles around their mean. Thus, depth and width reflect the geometric span of a cluster, whereas spread captures the distribution of energy within that span.

Fig. 5 illustrates the CDF of the delay depth, angular width, and the corresponding fitted models. For the delay depth, the four cases exhibit the ranges of $[0.005, 17.73]$ ns, $[0.01, 12.53]$ ns, $[0.005, 11.03]$ ns, and $[0.01, 10.74]$ ns with

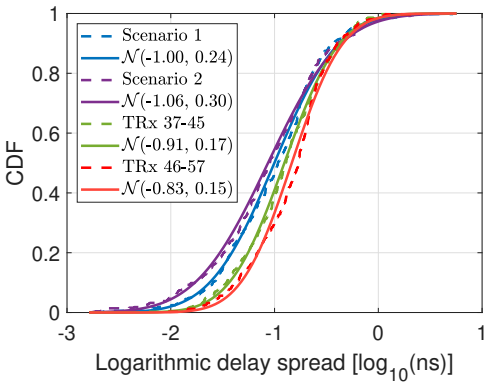

(a)

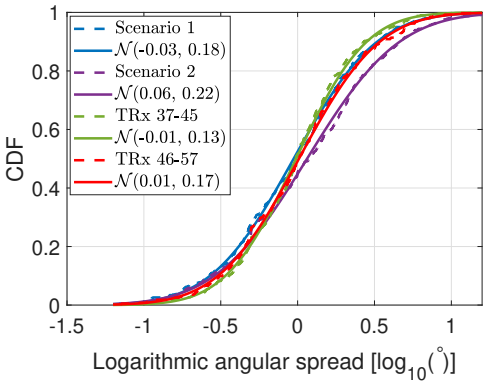

(b)

Fig. 6. The CDF of the logarithmic intra-cluster delay spreads, logarithmic angular spreads, and the fitted models. (a) Delay spreads. (b) Angular spreads.

the corresponding average values of 0.89, 1.00, 1.16, and 1.47 ns, respectively. As shown in Fig. 5 (a), the CDFs of the delay depths for the four cases, plotted on a logarithmic scale, closely follow normal distributions. In terms of angular width, the four cases demonstrate a range of values spanning $[1°, 136°]$, $[1°, 120°]$, $[1°, 104°]$, and $[1°, 117°]$, respectively. The corresponding average angular widths are $8.83°$, $9.71°$, $8.28°$, and $10.81°$, respectively. In Fig. 5 (b), it can be found that the logarithmic angular widths in these four cases are fitted well with the normal distributions. Besides, it is observed in Fig. 4 that Scenario 2 yields the largest number of MPC clusters; however, it does not exhibit the largest delay depth in Fig. 5, since the numerous metallic pillars in this scenario generate predominantly specular reflections, resulting in clusters whose MPCs contain minimal diffuse components and occupy only a narrow delay–angle region. Consequently, despite the high cluster count, the intra-cluster delay span remains small.

The intra-cluster delay and angular spreads are key parameters used to characterize the dispersion of MPCs within a cluster in the delay and angle domains, respectively. The delay and angular spreads characterize the statistical dispersion of MPCs within a cluster. In contrast, delay depth and angular width refer to the absolute range of the cluster in the delay and angle domains. Both metrics provide complementary insights, i.e., depth and width reflect the geometric extent of MPCs in the channel, while spreads capture the distribution of energy, which is critical for accurate channel modeling and ISAC system design. Detailed definitions and formulations can be found in [47]–[49] for the detailed explanation and equations of the delay and angular spreads. Fig. 6 presents the CDFs of delay and angular spreads, along with their respective fitted distribution models. Regarding the intra-cluster delay spread, Scenario 2 exhibits the smallest spread, with an average value of 0.17 ns. In comparison, Scenario 1 and TRxs 37-45 both show slightly larger average spreads of 0.18 ns. TRxs 46-57 display the largest intra-cluster delay spread among the four cases, with a mean value of 0.21 ns. The corresponding ranges of delay spreads are $[0, 2.94]$, $[0, 5.24]$, $[0, 1.20]$, and $[0, 2.60]$ ns, respectively. Similar to the analysis of delay depth and angular width, normal distributions are fitted to the logarithmic intra-cluster delay spreads, showing a strong agreement between the empirical data and the fitted models, as depicted in Fig. 6 (a). In terms of the intra-cluster angular spreads, the angular spreads of these four cases show a very close values, with the range of $[0°, 10.78°]$, $[0°, 25.65°]$, $[0°, 13.64°]$, and $[0°, 22.56°]$, respectively. The corresponding mean angular spreads are $1.40°$, $1.71°$, $1.27°$, and $1.48°$, respectively. In Fig. 6(b), normal distribution fitting is also applied to the CDF of the logarithmic intra-cluster angular spreads, showing a good match between the fitted model and the empirical data.

V. Environment-Aware Sensing Channel Modeling Framework

This section introduces an environment-aware channel modeling framework for monostatic sensing, which establishes a mapping between the physical characteristics of the environment and the channel features. Fig. 7 illustrates the proposed environment-aware channel modeling framework. Besides, a summary of the proposed framework, linking measurable channel observables to inferred physical attributes, is provided in Table III. Specifically, the quantity and spatial distribution of reflectors influence the number of MPC clusters and their delay-angle information, as more complex environments tend to generate a greater number of distinguishable reflection groups. Surface roughness impacts both the number and angular span of diffuse MPCs within each cluster, i.e., rougher surfaces scatter energy more broadly. Besides, the surface roughness can be characterized using power distribution in the angle domain, i.e., the Lambertian model. Reflector geometry further shapes the spatial arrangement of MPCs, influencing cluster boundaries and intra-cluster dispersion patterns, depending on the physical layout (e.g., a flat wall or a corner). Material type are manifested in the reflection loss distribution between specular and diffuse components, which is governed by the electromagnetic (EM) properties of different materials. Note that in this work, the TRx-to-reflector distance is fixed at 1.2 m across all scenarios to maintain consistent geometric conditions when isolating material-related effects. In practical sensing deployments, the TRx-reflector distance may vary or be unknown; however, its influence on the derived parameters can be calibrated or compensated for during processing

TABLE III
SUMMARY OF THE PROPOSED SENSING CHANNEL MODELING FRAMEWORK

Level	Physical Feature	Key Propagation Observables	Main Output
1	Reflector quantity & location	Number of MPC clusters & cluster delay and angle centroids from high-resolution parameter estimation	Spatial distribution and count of dominant reflectors
2	Surface roughness	Number of diffuse MPCs within each cluster & Lambertian model	Relative roughness classification and scattering strength
3	Reflector geometry	Spatial distribution of MPCs & intra-cluster delay-angle dispersions;	Geometric categorization of reflectors
4	Material type	Specular and diffuse reflection loss distributions	Material identification and EM property estimation

(e.g., in reflection loss estimation). While the Lambertian scattering model is generally stable under small distance variations, larger changes in range may alter the effective scattering geometry, which warrants further investigation in future work. The fixed-distance configuration adopted here, therefore, serves as a controlled reference for subsequent studies considering variable-distance scenarios.

These four physical features can be ranked by the level of inference difficulty in THz monostatic sensing. The easiest to extract is the reflector quantity and location (Level 1), which can be reliably identified using high-resolution parameter estimation algorithms that extract delay and angle information of MPC clusters [33], [50]. Surface roughness (Level 2) follows, as the short wavelengths at THz frequencies make the system highly sensitive to fine surface textures. This enables the detection of scattering behavior associated with rough surfaces, as demonstrated in several recent studies [51]–[53]. Reflector geometry (Level 3) poses a greater challenge, as it requires spatial interpretation of the shape and angular distribution of clustered diffuse MPCs. However, the pronounced surface scattering at THz frequencies, resulting from sub-millimeter wavelengths, makes it possible to infer reflector shapes such as corners and curved surfaces [17]. The most difficult task is the identification of material type (Level 4), which involves distinguishing between different materials based on their specular and diffuse reflection behavior. This requires accurate statistical modeling, which forms a key contribution of this work. The detailed analysis of these features is provided in the following subsection.

By explicitly connecting these hierarchical physical attributes to observable propagation features, the proposed environment-aware modeling framework enables more accurate and interpretable THz channel representations tailored for sensing-aware applications. The following subsections provide a detailed investigation of key material-related features, namely, surface roughness, reflector geometry, and material composition.

A. Surface Roughness

Surface roughness is a crucial physical property of reflectors, particularly at THz frequencies, where the wavelength is on the order of millimeters. At such short wavelengths, even small surface irregularities can significantly affect wave scattering, making THz signals susceptible to surface texture.

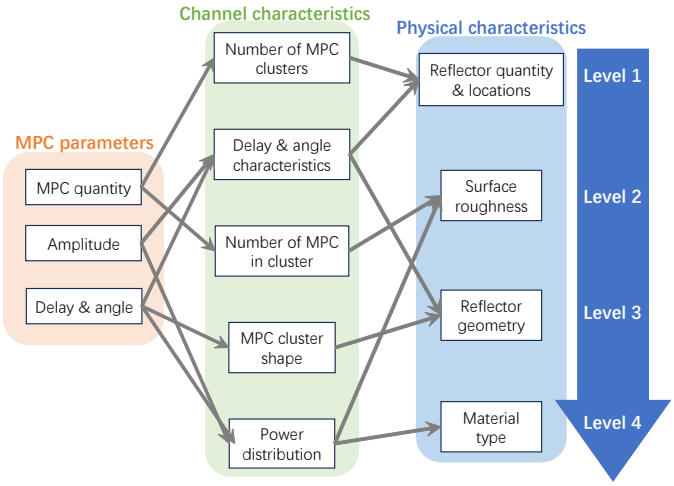

Fig. 7. The framework of the environment-aware channel modeling for monostatic sensing.

Roughness can be quantified by the root mean square (RMS) height σ of the surface profile [54], defined as

$$\sigma = \sqrt{\frac{1}{N}\sum_{i=1}^{N}\left(h_i - \bar{h}\right)^2}, \tag{13}$$

where h_i is the measured height at the i-th point, $\bar{h}$ is the mean height, and N is the total number of sampled points.

In practical channel measurements, obtaining σ is often infeasible in non-invasive scenarios. Thus, in this work, we employ two empirically driven indicators to infer roughness effects indirectly: (i) the number of detected MPCs within a cluster and (ii) the angular spread of reflections modeled using Lambertian-like behavior. To illustrate the first indicator, Fig. 8 presents delay-angle profiles for reflections from flat walls made of polymer, cement, and tile materials with progressively smoother surfaces based on visual inspection and construction standards. The observed angular spans are 110° (polymer), 106° (cement), and 90° (tile), and the corresponding numbers of detected MPCs are 267, 195, and 99, respectively. These results reveal a clear trend: surfaces with greater roughness tend to produce broader angular dispersion and a larger number of diffuse multipath reflections.

The Lambertian model is also a metric to analyze the surface roughness. According to the Lambertian model [55], the diffuse power $p_{\mathrm{Lam}}(\Delta\theta)$ is proportional to $\cos^2(\Delta\theta)$

$$p_{\mathrm{Lam}}(\Delta\theta) = n_{\mathrm{Lam}} \cdot \cos^2(\Delta\theta) + b_{\mathrm{Lam}}, \tag{14}$$

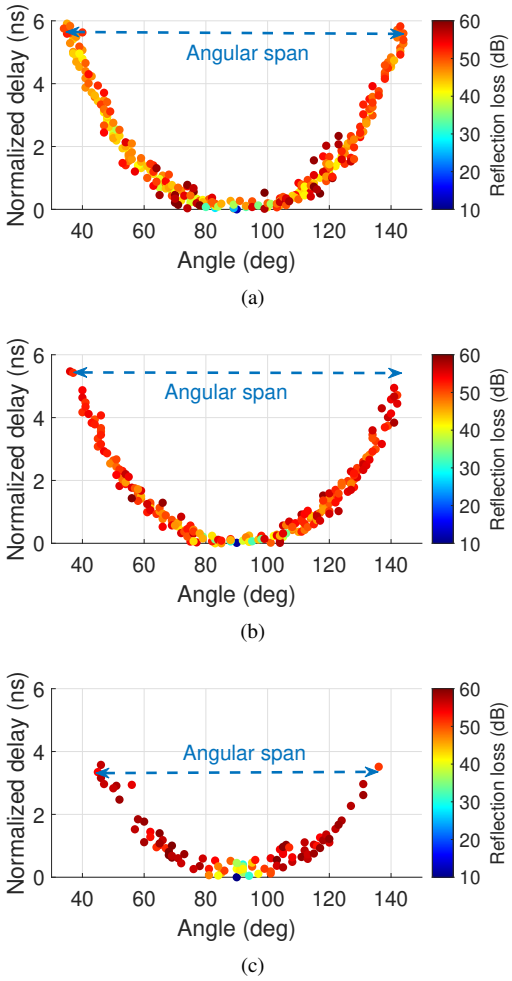

Fig. 8. The reflected MPCs from flat walls composed of three materials with varying roughness. (a) Polymer. (b) Cement. (c) Tile.

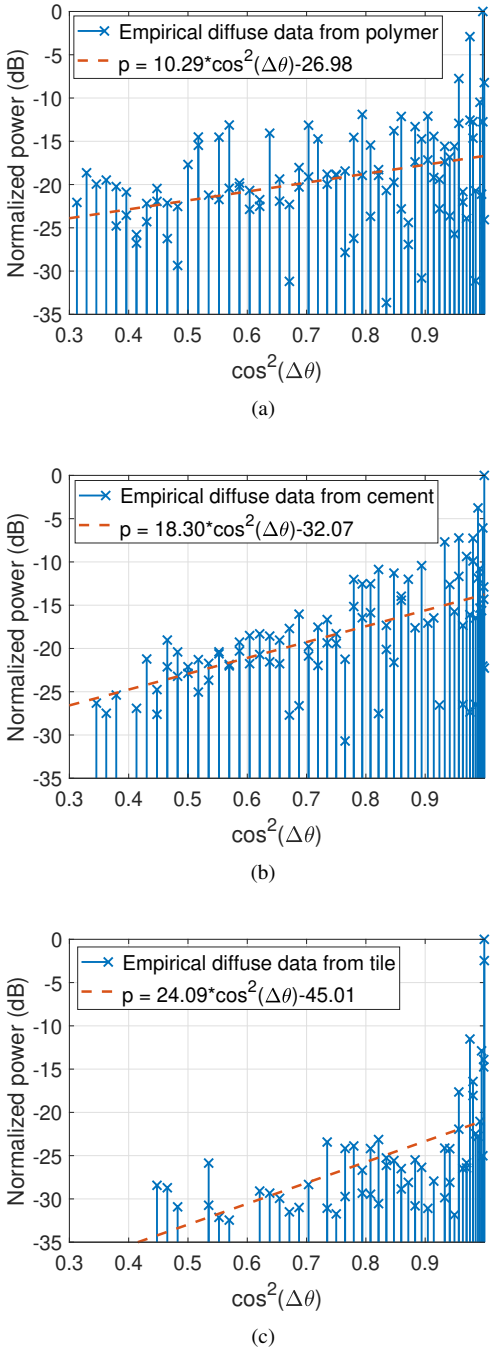

Fig. 9. The relationship between the diffuse power with $\cos^2(\Delta\theta)$ and the fitted Lambertian model. (a) Polymer. (b) Cement. (c) Tile.

where $\Delta\theta$, n_{Lam}, and b_{Lam} are the angle difference between the diffuse angle θ_{diff} and the specular reflection angle θ_{spec}, i.e., $\Delta\theta = \theta_{\text{spec}} - \theta_{\text{diff}}$, the slope of the diffuse power compared to $\cos^2(\Delta\theta)$, and the intercept. Note that the diffuse power $p_{\text{Lam}}(\Delta\theta)$ is obtained by summing the powers of all diffuse MPCs arriving at the same angle θ_{diff}.

Fig. 9 illustrates the comparison between the normalized diffuse power and the corresponding fitted Lambertian scattering models for three surfaces with varying roughness. It can be observed that the diffuse power generally increases with $\cos^2(\Delta\theta)$, consistent with the Lambertian scattering principle. The fitted Lambertian models for the polymer, cement, and tile surfaces are $p_{\text{Lam}}(\Delta\theta) = 10.29 \cdot \cos^2(\Delta\theta) - 26.98$ dB, $p_{\text{Lam}}(\Delta\theta) = 18.30 \cdot \cos^2(\Delta\theta) - 32.07$ dB, and $p_{\text{Lam}}(\Delta\theta) = 24.09 \cdot \cos^2(\Delta\theta) - 45.01$ dB, respectively. These results reveal a clear trend: as the surface roughness increases, the slope parameter n_{Lam}, representing the degree of angular concentration in the Lambertian fit, decreases. This implies that rougher surfaces yield more widely dispersed diffuse scattering, while smoother surfaces concentrate the diffuse energy more narrowly around the specular direction.

Note that the surface roughness classification in this study is primarily based on empirical observations rather than precise surface measurements. Nevertheless, it provides a practical and intuitive interpretation that aligns with expected surface-scattering behavior at high frequencies. Besides, the Lambertian model remains suitable for surfaces with moderate roughness or thin coatings, where the averaged diffuse scattering still exhibits a quasi-Lambertian response. For highly irregular or multi-layered materials, the model may be enhanced by incorporating multi-slope or composite formulations to capture directional scattering features or layer-specific reflections.

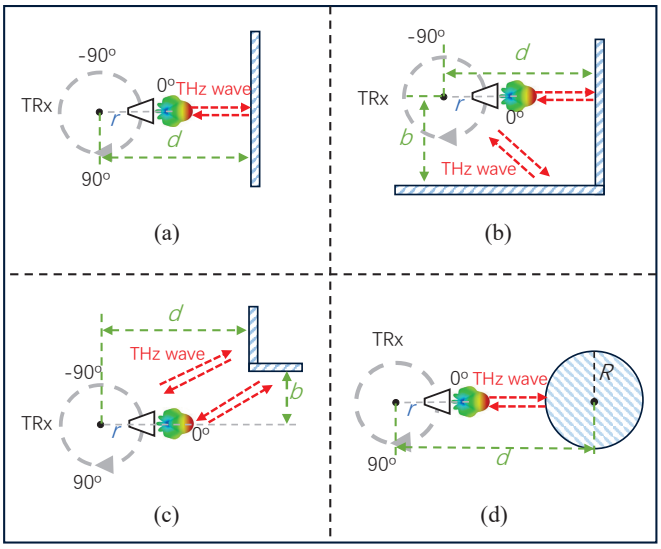

Fig. 10. The layout of the indoor representative physical structures. (a) Flat wall. (b) Concave corner. (c) Convex corner (d) Cylinder pillar.

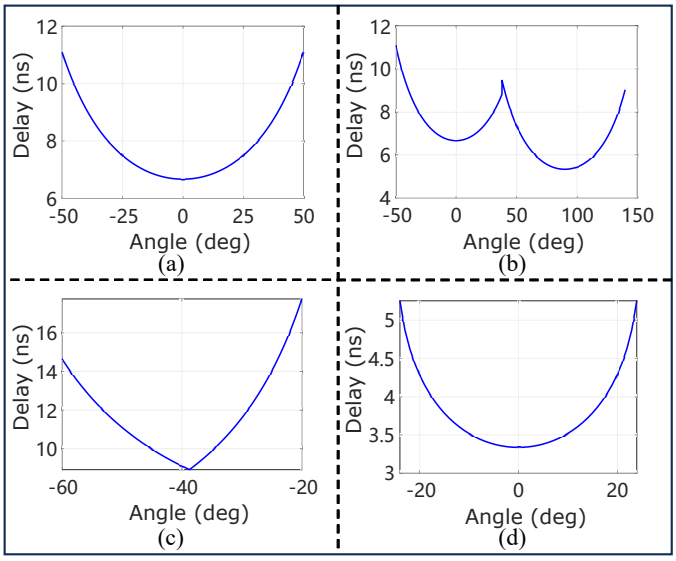

Fig. 11. The simulated structural model of different physical structures: (a) Flat wall. (b) Concave corner. (c) Convex corner (d) Cylinder pillar.

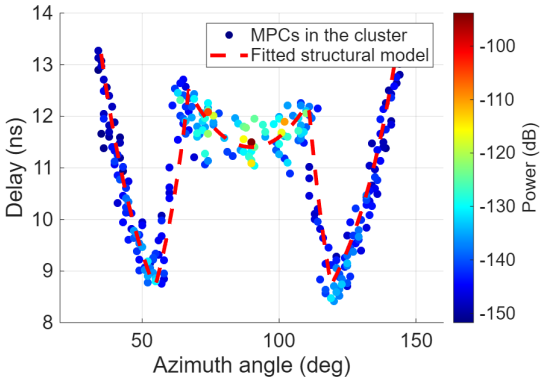

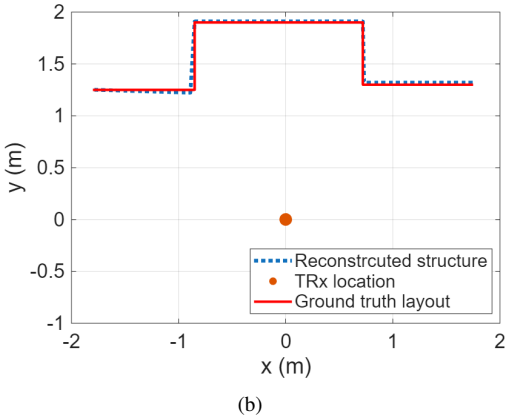

Fig. 12. Analysis of structural modeling using empirical data. (a) Example of matching a diffuse MPC cluster with the fitted structural model; (b) Reconstructed environment based on the identified structures.

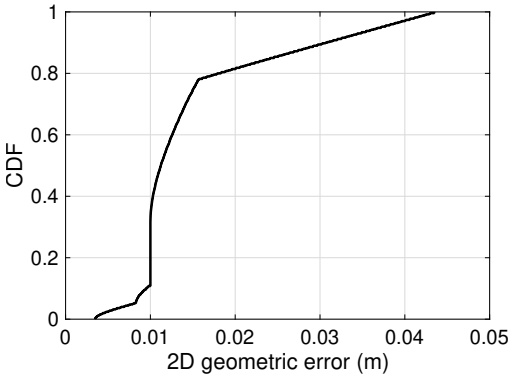

Fig. 13. The geometric error between the measured MPC and the fitted structure.

B. Reflector Geometry

In this subsection, two key parameters, i.e., cluster shape and material-specific channel dispersion, are analyzed, as these parameters reflect the geometry and structural characteristics of the reflectors.

1) Cluster Shape Analysis: The diffuse MPCs within a cluster can be effectively utilized to analyze the structural characteristics of reflectors. By examining the spatial distribution and geometric shape of these components, it becomes possible to infer the underlying physical structure of the reflecting objects. In this subsection, we investigate several representative physical structures, namely, a flat wall, a concave corner, a convex corner, and a cylindrical pillar, and analyze their corresponding manifestations in the channel as illustrative examples. The layout of these structures is depicted in Fig. 10. The corresponding delay-angle patterns are obtained through MATLAB simulations using a simple geometry-based analytical model, in which the azimuth angle is defined by the reflector layout and the round-trip delay is computed from the geometric path length. In the simulation setup, same as the measurements, the TRx moves along a circular trajectory with a radius of $r = 0.2$ m relative to the rotation center, and the distance to the reflectors is fixed at $d = 1.2$ m. For both the concave and convex corner scenarios, the distance b is set to 1.0 m. In the cylindrical pillar case, the pillar radius is configured as $R = 0.5$ m. All other simulation

parameters are aligned with the real measurement settings to ensure consistency. Fig. 11 presents the simulation results, showing how these different physical structures are manifested in the delay–angle domain. It can be clearly observed that each structure exhibits distinct channel characteristics, allowing for effective differentiation of reflector shapes based on their channel signatures.

By matching a structural model with the diffuse MPCs within a cluster, the structural characteristics of the reflector can be effectively identified. To obtain these reconstructed structures, we apply a geometry-based inversion procedure using the delay-angle pairs (τ_ℓ, θ_ℓ) extracted from the measured MPCs. For each MPC, the corresponding reflection distance is computed as $d_\ell = c\tau_\ell/2$, and several candidate geometric models (e.g., flat wall, corner, pillar) are examined by comparing the measured delay trajectory with the theoretical delay function $\tau_{\text{theo}}(\theta;\xi)$ associated with each model. The optimal structural parameters ξ^* are then obtained by minimizing the root-mean-square error between the measured and modeled delays, yielding the best-fitting reflector geometry. As an illustrative example, Fig. 12 presents the matching results for TRx 50, showing how the diffuse MPCs of a single cluster align with a fitted structural model. As depicted, two convex corners and one flat wall are identified, which correspond accurately to the actual layout in the measurement environment, as shown in the reconstructed structure in Fig. 12 (b). A comparison between the fitted structural model and the ground-truth geometry of Scenario 3 confirms a strong agreement. To quantify the reconstruction accuracy, the geometric error was evaluated and summarized using the mean error, maximum error, and root-mean-square error (RMSE). The corresponding CDF is shown in Fig. 13. The mean error is 0.02 m, the maximum error is 0.04 m, and the RMSE is 0.02 m, with more than 90% of the reconstructed points exhibiting errors below 0.02 m. These results demonstrate that the proposed reconstruction method achieves centimeter-level geometric accuracy.

2) Material-Specific Channel Dispersion: The intra-cluster delay and angular spreads can serve as indirect indicators of reflector geometry by capturing the spatial dispersion of multipath components resulting from interactions with physical surfaces. To analyze this, clusters associated with specific reflector materials are identified based on scenario geometry and specular reflection loss. Only clusters involving reflections from a single material type are considered.

Using Scenario 1 as an example, Fig. 14 presents the material-specific intra-cluster spreads. The delay spread ranges for cement, glass, and metal are observed as $[0.12, 0.80]$ ns, $[0.004, 0.66]$ ns, $[0.07, 0.40]$ ns, respectively. In terms of logarithmic angular spread, metal exhibits the narrowest range $[0°, 1.80°]$,, consistent with its small, localized structures (e.g., metallic window frames). Glass surfaces show a moderately wider spread $[0°, 7.79°]$, while cement surfaces yield the broadest spread $[2.33°, 10.41°]$, reflecting their larger physical extent and rougher texture, which induce wider angular dispersion. These trends suggest that larger reflectors produce more diffuse scattering, contributing to increased intra-cluster spreads. Moreover, the CDFs of both delay and angular spreads exhibit good agreement with fitted normal distributions, as shown in Fig. 14. It is also observed that the delay and angular spreads of metal and glass are relatively close in Fig. 14. This similarity arises due to the fact that in our measurement scenarios, both materials appear only over small, spatially confined regions (e.g., window frames or narrow glass panels), which limit the spatial extent of scattering and thus the resulting dispersion. In addition, both surfaces behave as smooth, predominantly specular reflectors at THz frequencies, further reducing temporal and angular spread variations. It is important to note that these dispersion metrics are used as auxiliary descriptors in our environment-aware modeling. The structural interpretation primarily relies on the geometric shape of the clusters in the delay–angle domain and their consistency with the theoretical structural models. Therefore, even when metal and glass yield similar intra-cluster spreads, the framework remains capable of capturing both material- and structure-dependent characteristics.

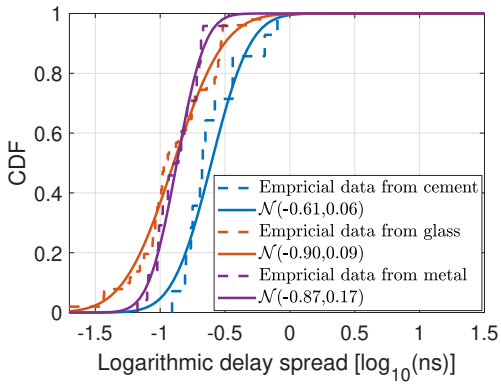

(a)

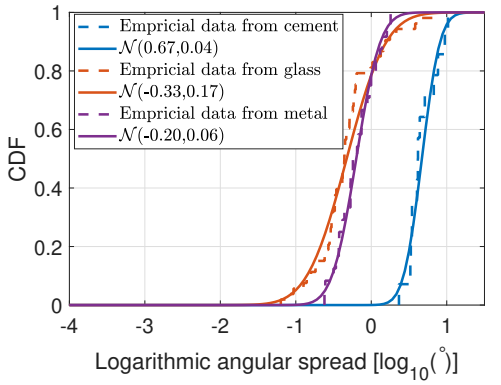

(b)

Fig. 14. The CDF of the material-specific intra-cluster delay and angular spreads, and the corresponding fitted models. (a) Delay spread. (b) Angular spread.

C. Material Type

As discussed in Section IV-A, specular and diffuse MPCs can be separated based on their reflection loss. As illustrated in [17], [18], material type can be inferred from the reflection loss characteristics. Therefore, in this subsection, we perform a comprehensive analysis and modeling of the reflection loss for

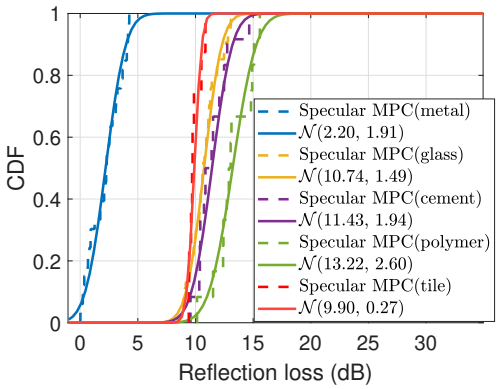

(a)

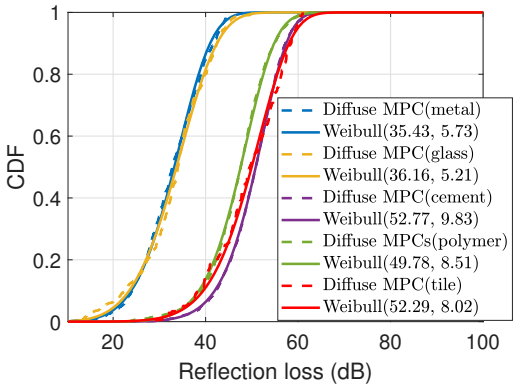

(b)

Fig. 15. The CDF of the reflection loss of the specular and diffuse MPCs, and the corresponding fitted models. (a) Specular MPCs. (b) Diffuse MPCs.

both specular and diffuse MPCs reflected from different materials. The MPC clusters associated with different materials are identified by correlating their parameters with the known geometric layout of the measurement scenarios. Note that this analysis focuses exclusively on MPC clusters reflected from a single material type, excluding those that involve reflections from multiple materials.

Fig. 15 presents the CDFs of the reflection loss for both specular and diffuse components, along with their corresponding fitted models. For the specular components, MPCs reflected from metal exhibit the lowest reflection loss, ranging from 0.03 to 4.25 dB. Specular reflections from the tile wall show a reflection loss in the range of $[9.41, 10.86]$ dB. The materials glass and cement exhibit comparable reflection loss characteristics, with ranges of $[9.26, 12.50]$ dB and $[10.56, 14.66]$ dB, respectively. Among all the tested materials, polymer demonstrates the highest specular reflection loss, ranging from 11.50 to 15.58 dB. As shown in Fig. 15 (a), the CDFs of specular reflection losses for all materials closely match the fitted normal distributions. Furthermore, the mean reflection losses of specular MPCs for various materials are compared with the material reflection loss database presented in [18] in Table IV, showing a strong agreement between measured and reference values. The two sets of results show close agreement across all tested materials, demonstrating a strong correspondence between intrinsic material properties and their propagation-based manifestations. Regarding the diffuse components, all diffuse MPCs exhibit higher reflection losses compared to their specular counterparts. The diffuse reflection losses for metal and glass are found to be similar, with ranges of $[15.97, 44.90]$ dB and $[15.19, 52.53]$ dB, respectively. In contrast, cement, polymer, and tile show comparable diffuse reflection losses, with ranges of $[24.97, 65.74]$ dB, $[23.63, 63.44]$ dB, and $[29.33, 60.99]$ dB, respectively. As illustrated in Fig. 15 (b), the diffuse reflection loss distributions align well with fitted Weibull models. The distinct statistical characteristics of reflection losses across different materials suggest the feasibility of data-driven material classification. For instance, the models of specular and diffuse reflection loss for various materials can serve as discriminative features for classifiers. A confusion-matrix-based analysis for more materials would be valuable for quantifying classification performance, which we leave for future exploration.

TABLE IV
COMPARISON OF REFLECTION LOSS FROM TDS MEASUREMENTS AND MEASURED SPECULAR REFLECTION LOSS

Material	Reflection Loss from TDS (dB)	Mean Specular Reflection Loss (dB)
Metal	2.42	2.20
Glass	9.76	10.47
Cement	11.84	11.43
Polymer	13.68	13.22
Tile	9.15	9.90

VI. CONCLUSION

In this work, channel measurements were carried out in three representative indoor scenarios to investigate THz monostatic sensing channels at the 300 GHz band. Using a SAGE-based parameter estimation algorithm, key MPC parameters, including amplitude, delay, and azimuth angle, were extracted and analyzed across scenarios. Building on these measurements, we proposed a hierarchical environment-aware modeling framework that links reflector quantity and location, surface roughness, geometry, and material type to their observable channel characteristics. The analysis demonstrates that this framework can reliably infer physical environmental attributes from channel-domain representations, providing a physically interpretable basis for THz ISAC channel modeling. The proposed framework is scalable to larger indoor and outdoor environments. Although MPC density varies with scene size and complexity, the hierarchical mapping between reflector properties and channel observables remains valid. By dividing large areas into locally homogeneous subregion and calibrating path-loss, scattering, and atmospheric parameters, the same modeling structure can be applied broadly. The framework is compatible with the stochastic models such as 3GPP TR 38.901. The extracted cluster parameters and material-dependent reflection characteristics can support future THz ISAC extensions above 100 GHz, improving physical realism in standardized models. Future work will integrate THz sensing with modalities such as vision and LiDAR to combine THz material awareness with geometric and semantic

information from optical sensors, enabling more robust multi-modal environment reconstruction in complex scenarios.

REFERENCES

[1] C.-X. Wang, X. You, X. Gao, X. Zhu, Z. Li, C. Zhang, H. Wang, Y. Huang, Y. Chen, H. Haas, J. S. Thompson, E. G. Larsson, M. D. Renzo, W. Tong, P. Zhu, X. Shen, H. V. Poor, and L. Hanzo, "On the road to 6G: Visions, requirements, key technologies, and testbeds," *IEEE Commun. Surveys Tuts.*, vol. 25, no. 2, pp. 905–974, 2023.

[2] Z. Ma, Y. Liang, Q. Zhu, J. Zheng, Z. Lian, L. Zeng, C. Fu, Y. Peng, and B. Ai, "Hybrid-RIS-assisted cellular ISAC networks for UAV-enabled low-altitude economy via deep reinforcement learning with mixture-of-experts," *IEEE Trans. Cogn. Commun. Netw.*, pp. 1–1, 2025.

[3] X. Cheng, H. Zhang, J. Zhang, S. Gao, S. Li, Z. Huang, L. Bai, Z. Yang, X. Zheng, and L. Yang, "Intelligent multi-modal sensing-communication integration: Synesthesia of machines," *IEEE Commun. Surv. Tutorials*, vol. 26, no. 1, pp. 258–301, 2024.

[4] L. Bai, M. Lu, Z. Huang, and X. Cheng, "A multi-modal uav-to-ground channel model for 6g intelligent sensing-communication integration," *IEEE Trans. Commun.*, pp. 1–1, 2025.

[5] C. Chaccour, W. Saad, O. Semiari, M. Bennis, and P. Popovski, "Joint sensing and communication for situational awareness in wireless THz systems," in *Proc. of IEEE ICC*, 2022, pp. 3772–3777.

[6] J. M. Jornet, H. Elayan, T. Nagatsuma, M. Juntti, E. T. R. Pinto, T. Kürner, H. Guerboukha, D. M. Mittleman, and E. Knightly, "Mobile terahertz communication and sensing systems: A future look," *IEEE Veh. Technol. Mag.*, vol. 19, no. 4, pp. 20–35, 2024.

[7] W. Jiang, Q. Zhou, J. He, M. A. Habibi, S. Melnyk, M. El-Absi, B. Han, M. D. Renzo, H. D. Schotten, F.-L. Luo, T. S. El-Bawab, M. Juntti, M. Debbah, and V. C. M. Leung, "Terahertz communications and sensing for 6G and beyond: A comprehensive review," *IEEE Commun. Surv. Tutorials.*, vol. 26, no. 4, pp. 2326–2381, 2024.

[8] X. Cai, X. Cheng, and F. Tufvesson, "Toward 6g with terahertz communications: Understanding the propagation channels," *IEEE Commun. Mag.*, vol. 62, no. 2, pp. 32–38, 2024.

[9] Z. Chen, C. Han, Y. Wu, L. Li, C. Huang, Z. Zhang, G. Wang, and W. Tong, "Terahertz wireless communications for 2030 and beyond: A cutting-edge frontier," *IEEE Commun. Mag.*, vol. 59, no. 11, pp. 66–72, 2021.

[10] FCC, "FCC opens spectrum horizons for new services and technologies," Mar. 2019. [Online]. Available: https://www.fcc.gov/document/fcc-opens-spectrum-horizons-new-services-technologies

[11] ETSI, "TeraHertz Technology (THz); Identification of Frequency Bands of Interest for THz Communication Systems," European Telecommunications Standards Institute, ETSI Group Report GR THz 002, 2024, ETSI ISG THz.

[12] ITU-R, "Resolution 663 (Rev. WRC-23): Possible Allocations for Active Services in the 231.5–275 GHz and 275–700 GHz Bands," International Telecommunication Union, Resolution, Nov. 2023, World Radiocommunication Conference (WRC-23).

[13] Y. Chen, Z. Yu, J. He, J. Li, and G. Wang, "A scatterer-based hybrid channel model for integrated sensing and communications (ISAC)," in *Proc. of IEEE PIMRC*, 2023, pp. 1–7.

[14] D. Dupleich, A. Ebert, Y. Völker-Schöneberg, D. Sitdikov, M. Boban, G. Del Galdo, and R. Thomä, "Characterization of propagation from measurements at sub-THz for ISAC applications in an emulated dynamic industrial scenario," in *Proc. of EuCAP*, 2024, pp. 1–5.

[15] Y. Li, Y. Wang, Y. Chen, Z. Yu, and C. Han, "300 GHz experiment-based ranging and mapping in indoor environments," in *Proc. of IEEE SPAWC*, 2023, pp. 396–400.

[16] M. Lotti, G. Pasolini, A. Guerra, F. Guidi, R. d'Errico, and D. Dardari, "Radio SLAM for 6G systems at THz frequencies: Design and experimental validation," *IEEE J. Sel. Top. Signal Process.*, vol. 17, no. 4, pp. 834–849, 2023.

[17] Y. Lyu, Z. Huang, S. Schwarz, and C. Han, "Hybrid channel modeling and environment reconstruction for terahertz monostatic sensing," *IEEE Trans. Wireless Commun.*, pp. 1–1, 2025.

[18] Z. Fang, Y. Lyu, Z. Yu, and C. Han, "Environment reconstruction in terahertz monostatic sensing: Joint millimeter-level geometry mapping and material identification," *IEEE J. Sel. Topics Electromagn. Antennas Propag.*, vol. 1, no. 1, pp. 265–277, 2025.

[19] C. Gentile, A. F. Molisch, J. Chuang, D. G. Michelson, A. Bodi, A. Bhardwaj, O. Ozdemir, W. A. G. Khawaja, I. Guvenc, Z. Cheng, F. Rottenberg, T. Choi, R. Müller, N. Han, and D. Dupleich, "Methodology for benchmarking radio-frequency channel sounders through a system model," *IEEE Trans. Wireless Commun.*, vol. 19, no. 10, pp. 6504–6519, 2020.

[20] J. Zhang, J. Lin, P. Tang, Y. Zhang, H. Xu, T. Gao, H. Miao, Z. Chai, Z. Zhou, Y. Li *et al.*, "Channel measurement, modeling, and simulation for 6G: A survey and tutorial," *arXiv preprint arXiv:2305.16616*, 2023.

[21] N. González-Prelcic, M. Furkan Keskin, O. Kaltiokallio, M. Valkama, D. Dardari, X. Shen, Y. Shen, M. Bayraktar, and H. Wymeersch, "The integrated sensing and communication revolution for 6g: Vision, techniques, and applications," *Proceedings of the IEEE*, vol. 112, no. 7, pp. 676–723, 2024.

[22] L. Pucci, E. Paolini, and A. Giorgetti, "System-level analysis of joint sensing and communication based on 5G new radio," *IEEE J. Sel. Areas Commun.*, vol. 40, no. 7, pp. 2043–2055, 2022.

[23] C. Baquero Barneto, E. Rastorgueva-Foi, M. F. Keskin, T. Riihonen, M. Turunen, J. Talvitie, H. Wymeersch, and M. Valkama, "Millimeter-wave mobile sensing and environment mapping: Models, algorithms and validation," *IEEE Trans. Veh. Technol.*, vol. 71, no. 4, pp. 3900–3916, 2022.

[24] Z. Cui and S. Pollin, "Extracting the communication channel from monostatic sensing channels: From propagation to impact analysis," *IEEE Trans. Antennas Propag.*, vol. 73, no. 8, pp. 6193–6198, 2025.

[25] Y. Liu, J. Zhang, Y. Zhang, Z. Yuan, and G. Liu, "A shared cluster-based stochastic channel model for integrated sensing and communication systems," *IEEE Trans. Veh. Technol.*, vol. 73, no. 5, pp. 6032–6044, 2024.

[26] Y. Wang, T. Wang, X. Zheng, X. Hao, and X. Liao, "Millimeter-wave and sub-THz radio propagation channel measurements and modeling in an indoor factory environment for ISAC," *IEEE Trans. Antennas Propag.*, vol. 73, no. 9, pp. 6883–6898, 2025.

[27] Z. Ma, R. Zhang, B. Ai, Z. Lian, L. Zeng, D. Niyato, and Y. Peng, "Deep reinforcement learning for energy efficiency maximization in RSMA-IRS-assisted ISAC system," *IEEE Trans. Veh. Technol.*, pp. 1–6, 2025.

[28] F. Taleb, G. G. Hernandez-Cardoso, E. Castro-Camus, and M. Koch, "Transmission, reflection, and scattering characterization of building materials for indoor THz communications," *IEEE Trans. Terahertz Sci. Technol.*, vol. 13, no. 5, pp. 421–430, 2023.

[29] N. B. Refvik, C. E. Jensen, D. N. Purschke, W. Pan, H. R. J. Simpson, W. Lei, R. Gu, J. Antoszewski, G. A. Umana-Membreno, L. Faraone, and F. A. Hegmann, "Noncontact characterization of carrier mobility in long-wave infrared hgcdte films with terahertz time-domain spectroscopy," *IEEE Trans. Terahertz Sci. Technol.*, vol. 14, no. 4, pp. 466–475, 2024.

[30] C. Jansen, R. Piesiewicz, D. Mittleman, T. Kurner, and M. Koch, "The impact of reflections from stratified building materials on the wave propagation in future indoor terahertz communication systems," *IEEE Trans. Antennas Propag.*, vol. 56, no. 5, pp. 1413–1419, 2008.

[31] T. Kleine-Ostmann, R. Piesiewicz, N. Krumbholz, D. Mittleman, T. Kurner, and M. Koch, "Characterization of building materials for the modeling of pico-cellular thz communication systems," in *Proc. of 30th IRMMW-THz*, vol. 2, 2005, pp. 592–593 vol. 2.

[32] Y. Lyu, P. Kyösti, and W. Fan, "Sub-THz VNA-based channel sounder structure and channel measurements at 100 and 300 GHz," in *Proc. of PIMRC*, 2021, pp. 1–5.

[33] Y. Li, C. Han, Y. Chen, Z. Yu, and X. Yin, "DSS-o-SAGE: Direction-scan sounding-oriented SAGE algorithm for channel parameter estimation in mmWave and THz bands," *IEEE Trans. Antennas Propagat.*, pp. 1–1, 2024.

[34] S. Velasco-Forero and J. Angulo, "Random projection depth for multivariate mathematical morphology," *IEEE J. Sel. Topics Signal Process.*, vol. 6, no. 7, pp. 753–763, 2012.

[35] M. Xiao, H. Wang, Z. Zeng, and Y. Bie, "SAR image segmentation and target detection based on mathematical morphology," in *Proc. of 2nd CISS*, 2021, pp. 1–5.

[36] J. Y. Gil and R. Kimmel, "Efficient dilation, erosion, opening, and closing algorithms," *IEEE Trans. Pattern Anal. Mach. Intell.*, vol. 24, no. 12, pp. 1606–1617, 2002.

[37] J. Cui, Y. Song, H. Jiang, C. Wang, M. Zhang, G. Liu, D. Li, J. Zhao, J. Liu, Y. Su, W. Liu, P. Li, D. M. Mittleman, F. Song, and J. Ma, "Measurement and modeling on terahertz channel propagation through vegetation," *IEEE Trans. Terahertz Sci. Technol.*, vol. 15, no. 4, pp. 582–595, 2025.

[38] G. Guo, X. Yang, Y. Zhou, and N. Ma, "Diffuse scattering analysis of indoor propagation channel at terahertz frequency," in *Proc. of 2024 IEEE WCNC*, 2024, pp. 1–6.

[39] R. Pan, D. He, K. Guan, B. Peng, J. Dou, L. Guo, Z. Zhong, and T. Kürner, "Terahertz channel modeling based on scattering characterization," in *Proc. of 18th EuCAP*, 2024, pp. 1–5.

[40] J. M. Eckhardt, T. Doeker, and T. Kürner, "Hybrid channel model for low terahertz links in a data center," *IEEE Open J. Commun. Soc.*, vol. 5, pp. 4731–4745, 2024.

[41] Y. Wang, Y. Lil, Y. Chen, Z. Yu, and C. Han, "Terahertz channel measurement and analysis on a university campus street," in *Proc. of IEEE ICC 2023*, 2023, pp. 2075–2080.

[42] Y. Chen, C. Han, J. He, and G. Wang, "A framework of Mahalanobis-distance metric with supervised learning for clustering multipath components in mimo channel analysis," *IEEE Trans. Antennas Propag.*, vol. 70, no. 6, pp. 4069–4081, 2022.

[43] X. Liu, J. Zhang, P. Tang, L. Tian, H. Tataria, S. Sun, and M. Shafi, "Channel sparsity variation and model-based analysis on 6, 26, and 105 GHz measurements," *IEEE Trans. Veh. Technol.*, vol. 73, no. 7, pp. 9387–9397, 2024.

[44] D. Shakya, S. Ju, O. Kanhere, H. Poddar, Y. Xing, and T. S. Rappaport, "Radio propagation measurements and statistical channel models for outdoor urban microcells in open squares and streets at 142, 73, and 28 GHz," *IEEE Trans. Antennas Propag.*, vol. 72, no. 4, pp. 3580–3595, 2024.

[45] R. He, B. Ai, A. F. Molisch, G. L. Stuber, Q. Li, Z. Zhong, and J. Yu, "Clustering enabled wireless channel modeling using big data algorithms," *IEEE Commun. Mag.*, vol. 56, no. 5, pp. 177–183, 2018.

[46] A. F. Molisch, K. Balakrishnan, C.-C. Chong, S. Emami, A. Fort, J. Karedal, J. Kunisch, H. Schantz, U. Schuster, and K. Siwiak, "IEEE 802.15. 4a channel model-final report," *IEEE P802*, vol. 15, no. 04, p. 0662, 2004.

[47] S. Ju, D. Shakya, H. Poddar, Y. Xing, O. Kanhere, and T. S. Rappaport, "142 GHz sub-terahertz radio propagation measurements and channel characterization in factory buildings," *IEEE Trans. Wireless Commun.*, vol. 23, no. 7, pp. 7127–7143, 2024.

[48] B. Fleury, "First- and second-order characterization of direction dispersion and space selectivity in the radio channel," *IEEE Trans. Inform. Theory*, vol. 46, no. 6, pp. 2027–2044, 2000.

[49] 3GPP, "Study on channel model for frequencies from 0.5 to 100 GHz," 3GPP, Tech. Rep. V17.0.0, March 2022.

[50] K.-W. Kim, M.-D. Kim, J.-J. Park, J. Lee, and H.-K. Kwon, "Sub-terahertz channel characterization in a lecture room from measurements with phase drift by a rotating horn antenna," *IEEE Trans. Antennas Propag.*, vol. 73, no. 2, pp. 1110–1124, 2025.

[51] X. Liao, C. Lin, X. Zheng, Y. Wang, and H. Song, "Measurements and modeling of depolarization characteristics from rough surfaces at Sub-THz band for indoor short-range communications," *IEEE Antennas Wirel. Propag. Lett.*, vol. 23, no. 12, pp. 4802–4806, 2024.

[52] X. Zhao, B. Chen, K. Guan, B. Lu, Y. Wei, and M. Dong, "Polarization characterization of thz scattering from rough surfaces based on deep learning," in *Proc. of 4th AT-RASC*, 2024, pp. 1–4.

[53] S. T. Gassel, M. R. Hofmann, and C. Brenner, "Influence of surface roughness on material classification for reflective THz-TDS measurements," in *Proc. of 48th IRMMW-THz*, 2023, pp. 1–2.

[54] H. Yi, K. Guan, P. T. Mathiopoulos, P. Xie, D. He, J. Dou, and Z. Zhong, "Full-wave simulation and scattering modeling for terahertz communications," *IEEE Journal of Selected Topics in Signal Processing*, vol. 17, no. 4, pp. 713–728, 2023.

[55] V. Degli-Esposti, F. Fuschini, E. M. Vitucci, and G. Falciasecca, "Measurement and modelling of scattering from buildings," *IEEE Trans. Antennas Propagat.*, vol. 55, no. 1, pp. 143–153, 2007.